APPLIED SCIENCES AND ENGINEERING

Robust nanogenerators based on graft copolymers via control of dielectrics for remarkable output power enhancement

Jae Won Lee,[1]* Hye Jin Cho,[2]* Jinsung Chun,[1] Kyeong Nam Kim,[1] Seongsu Kim,[3] Chang Won Ahn,[4] Ill Won Kim,[4] Ju-Young Kim,[1] Sang-Woo Kim,[3,5] Changduk Yang,[2†] Jeong Min Baik[1†]

A robust nanogenerator based on poly(*tert*-butyl acrylate) (PtBA)–grafted polyvinylidene difluoride (PVDF) copolymers via dielectric constant control through an atom-transfer radical polymerization technique, which can markedly increase the output power, is demonstrated. The copolymer is mainly composed of α phases with enhanced dipole moments due to the π-bonding and polar characteristics of the ester functional groups in the PtBA, resulting in the increase of dielectric constant values by approximately twice, supported by Kelvin probe force microscopy measurements. This increase in the dielectric constant significantly increased the density of the charges that can be accumulated on the copolymer during physical contact. The nanogenerator generates output signals of 105 V and 25 μA/cm^2, a 20-fold enhancement in output power, compared to pristine PVDF–based nanogenerator after tuning the surface potential using a poling method. The markedly enhanced output performance is quite stable and reliable in harsh mechanical environments due to the high flexibility of the films. On the basis of these results, a much faster charging characteristic is demonstrated in this study.

INTRODUCTION

Dielectric materials, commonly referred to as electrical insulators, have received much attention owing to their strong electron bonding, good support of electric fields, and low energy loss (*1*–*3*). In particular, the polarization and depolarization that occur in dielectrics as a result of an external electric field have been investigated as a means to efficiently charge and discharge electricity. This capability is very useful when applied to capacitors (*4*–*6*). Dielectrics have also been widely used in many applications, such as transistors (*7*, *8*), photovoltaic devices (*9*, *10*), and electrical insulation (*11*).

Recently, the triboelectric nanogenerator (TENG), which converts mechanical energy into electricity, has been suggested as a new energy-harvesting technology. Since 2012, it has been proven as a cost-effective, simple, and efficient technique for the realization of various self-powered systems, such as sensors (*12*, *13*) and charging systems (*14*, *15*). However, greater output performance is essential for the implementation of TENG in practical applications. Although various strategies to enhance the output performance have been reported, an effective dielectric for creating the device with high performance should be developed because the output power is critically dependent on the density of the charges transferred (*16*, *17*). To date, various dielectric materials, such as polydimethylsiloxane (PDMS) (*18*), poly(methyl methacrylate) (PMMA) (*19*), polyimide (PI) (*20*), polyvinylidene difluoride (PVDF) (*21*), and polytetrafluoroethylene (PTFE) (*22*), have been used without any modifications, and the resulting electrical signals were extremely weak. Very recently, modification of properties, such as compressibility (*16*), surface potential (*23*), and hydrophobicity (*24*), in a few TENGs has been reported; however, most of them have focused of partial reports of the effects of output performance. The parameters mentioned above may also be interrelated to each other. Therefore, the establishment of an interrelated library for the development of dielectrics from a materials perspective may be needed.

PVDF, a dielectric polymer with a good piezoelectric/pyroelectric response and low acoustic impedance, has been considered as one of the most widely studied dielectric materials in mechanical energy–harvesting technologies. In particular, it can be formed in a variety of nanostructures, such as nanowires, nanofibers, and nanotubes, and can be flexible; therefore, the use of PVDF has been successfully demonstrated in a number of devices, such as capacitors, sensors, and TENGs (*25*–*27*).

Following the principle that grafting one polymer onto another polymer backbone can combine the benefits of each parent polymer, we set out to design and synthesize PVDF graft copolymers to incorporate poly(*tert*-butyl acrylate) (PtBA) through an atom-transfer radical polymerization (ATRP) technique as an efficient dielectric to enhance the output performance of the TENGs. Grafting of PtBA onto the PVDF backbone suppressed the formation of the β phases; hence, the PVDF-G*n* graft copolymers were mainly composed of α phases. As the grafting ratio increased to 18%, the dielectric constant values increased from 8.6 to 16.5 in the frequency ranging from 10^2 to 10^5 Hz, which was attributed to the increase of the net dipole moment of the materials, and supported by the Kelvin probe force microscopy measurements (KPFMs). The TENG fabricated with the graft copolymer generated an output voltage of 64.4 V and a current density of 18.9 μA/cm^2, twice the enhancement in both, compared to pristine PVDF–based TENG. Further increase in the output performance to 105 V and 25 μA/cm^2, a 20-fold enhancement in output power, was also obtained by tuning the surface potential with the poling method, which improved the charge-accepting characteristics. The enhanced output performance was quite stable and reliable in a harsh mechanical environment due to the high flexibility of the

[1]School of Materials Science and Engineering, KIST-UNIST Ulsan Center for Convergent Materials, Ulsan National Institute of Science and Technology, Ulsan 44919, Republic of Korea. [2]Department of Energy Engineering, School of Energy and Chemical Engineering, Ulsan National Institute of Science and Technology, Ulsan 44919, Republic of Korea. [3]SKKU Advanced Institute of Nanotechnology, Sungkyunkwan University, Suwon 16419, Republic of Korea. [4]Department of Physics and Energy Harvest Storage Research Center, University of Ulsan, Ulsan 44610, Republic of Korea. [5]School of Advanced Materials Sciences and Engineering, Sungkyunkwan University, Suwon 16419, Republic of Korea.
*These authors contributed equally to this work.
†Corresponding author. Email: yang@unist.ac.kr (C.Y.); jbaik@unist.ac.kr (J.M.B.)

film. A much faster charging property was also demonstrated in this study.

RESULTS AND DISCUSSION

The PtBA-grafted PVDF copolymers were prepared with ATRP (Fig. 1A), in accordance with previously established methods in the literature (*28*). The grafting ratios were controlled as a function of various reaction times (12 to 72 hours) under the same conditions, yielding three samples with a different number-average molecular mass (M_n = 180.0 to 218.5 kDa). In a careful inspection of the ^{1}H nuclear magnetic resonance (NMR) spectra of the samples (Fig. 1B), the composition of the graft copolymers was calculated on a mole basis from the integral ratio of two noticeable resonances at 2.3 to 2.5 and 2.9 to 3.2 parts per million (ppm) attributed to head-to-head and head-to-tail configurations of PVDF and the signals at 1.4 to 1.65 ppm associated with the *tert*-butyl group in PtBA using the following equations (*29*)

$$x = \frac{(integral_{1.4-1.65})/9}{(integral_{2.3-2.5} + integral_{2.9-3.2})/2} \quad (1)$$

$$\text{PtBA mole percent (mol\%)} = \frac{x}{1+x} \times 100 \quad (2)$$

The mole percent of PtBA in the graft copolymer was determined as 10, 15, and 18%. Here, the graft copolymers were designated PVDF-G*n*, where G*n* refers to the mole percent of PtBA grafting. In addition, as shown in Fig. 1C, the Fourier transform infrared (FTIR) spectra of the PVDF-G*n* showed the appearance of the absorption bands at 1725 cm^{-1} assigned to the stretching vibrations of the ester carbonyl groups, in contrast with pristine PVDF. Also, as the grafting ratios of PtBA were increased, we observed the gradually enhanced intensity of the carbonyl bands relative to the methylene stretching bands of PVDF at about 1404 cm^{-1}, which further substantiates the PtBA content determined above.

As for a dielectric, the solutions were casted on a very flat SiO_2/Si substrate with a blocking layer. After the annealing process, the film

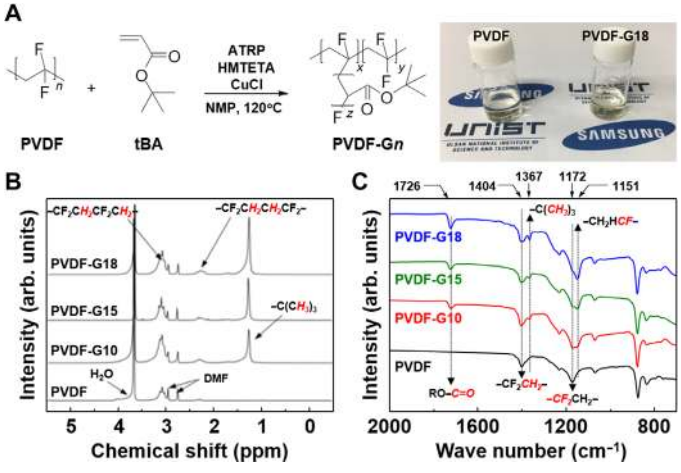

Fig. 1. Synthesis of PVDF-G*n* graft copolymers. (**A**) Synthesis of PVDF-G*n* graft copolymers and photograph of the PVDF and PVDF-G18 NMP solutions. ^{1}H NMR (**B**) and FTIR (**C**) of PVDF and PVDF-G*n*.

was peeled off from the substrate and glued on an Al film using a Kapton film, followed by the attachment of the Al electrode to fabricate the TENG, as shown in Fig. 2 (A and B). The detailed experimental procedures are also described in Materials and Methods. Figure 2B also shows that the resultant film appeared white and quite flexible after it was peeled off. The TENG had an active area of 2 cm × 2 cm, with the spacer between the bottom electrode and the PVDF-G*n* film made of four springs in each corner. The output voltages and current densities of the TENGs were measured and plotted in Fig. 2B and fig. S1. A cycled compressive force of around 50 N at an applied frequency of 10 Hz was applied. The TENG with pristine PVDF film showed small ac-type electrical output performance of less than approximately 32.9 V and 7.7 μA/cm^2. For the PVDF-G10, the output voltage and current density were increased to 45 V and 8.3 μA/cm^2, respectively. Furthermore, the highest enhancement (with an output voltage of 64.4 V and a current density of 18.9 μA/cm^2) was observed in PVDF-G18 under the same mechanical force. To show the high output performance of the TENG, we used various polymers, such as PI, PTFE, and polyvinyl chloride, as dielectrics in the TENGs and measured the electrical output performances. Figure S2 shows that the TENG with the PVDF-G18 film generated the largest output voltage and current density, compared with those with other polymers. The instantaneous power densities were also obtained by measuring the output voltages and current densities of the PVDF-G18–based TENG with external loads from 1 ohm to 1 gigohm, plotted in Fig. 2C. At 10 megohms, approximately 0.45 mA/cm^2 was obtained, a 20-fold enhancement in output power, compared with pristine PVDF–based TENG in fig. S3. The energy conversion efficiency of PVDF-G18–based TENG was estimated as the ratio between the output energy produced by the TENG and the input energy applied to the TENG. By considering the mass and the velocity of the top layer, the kinetic energy (that is, the input energy) was calculated to be 0.481 mJ. With an external load resistance of 10 megohms, the electrical energy produced by the TENG was approximately 0.054 mJ. Thus, the maximum energy conversion was calculated to be approximately 11.23%.

The transferred charge density of all samples significantly increased with the mole percent, showing agreement with the simulation and experimental results in Fig. 2D and figs. S4 and S5. According to a previous report (*16*), the dielectric constant of the dielectric plays a very important role in determining the electrical output performance of the TENG. The total transferred charge density (σ′) on the top electrode of the TENG can be expressed as (*30*)

$$\sigma' = \frac{-\sigma_0 d_{gap}}{d_{gap} + d_{PVDF}/\varepsilon_{PVDF}} \quad (3)$$

where σ_0 is the triboelectric charge density at the equilibrium state; d_{gap} and d_{PVDF} are the gap distance and thickness of PVDF-based films, respectively; and ε_{PVDF} is the dielectric constant of PVDF-based films. According to Eq. (3), the obtained σ′ can increase as the dielectric constant increases. Using the COMSOL Multiphysics software, we also calculated electrostatic potentials inside the TENG with PtBA mole percent, as shown in fig. S5. When the TENG is fully released, if we assume the electric potential (U_{bottom}) of the surfaces of the bottom layer to be zero, the electric potential of the surfaces of the top dielectric layer (U_{top}) can be expressed as $U_{top} = \sigma' d_{gap}/\varepsilon_0$, where σ′ is the total transferred charge density, ε_0 is the vacuum permittivity

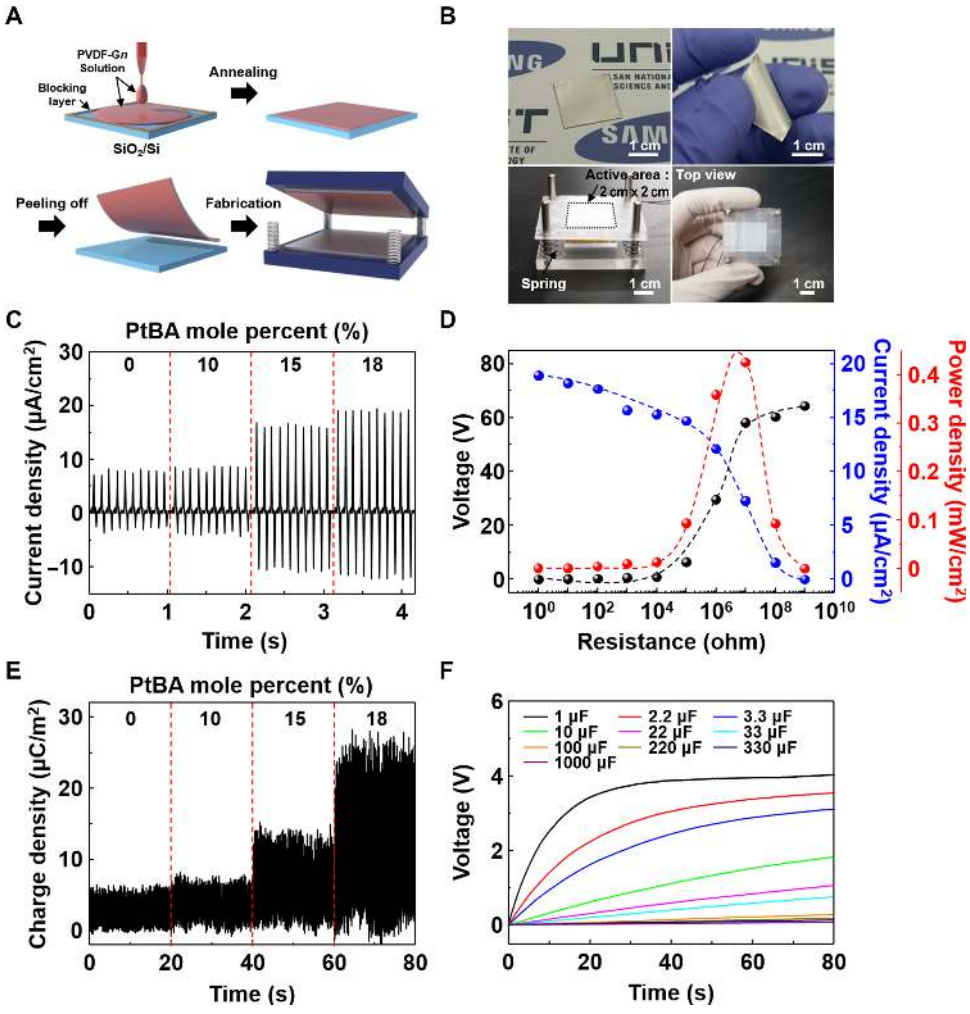

Fig. 2. Fabrication of PVDF-G*n*–based TENGs and its output performance. (**A**) Schematic diagrams of the fabrication process for the PVDF-G*n*–based TENGs. (**B**) Photographs of a flexible PVDF-G*n* film after it was peeled off and a PVDF-G*n*–based TENG. (**C**) Output current densities generated by the PVDF-based TENGs as a function of the PtBA mole percent ranging from 0 to 18%. (**D**) Output voltages, current densities, and output power densities of the PVDF-G18–based TENG with the resistance of external loads from 1 to 10^9 ohms. (**E**) Charge densities generated by the PVDF-based TENGs as a function of the PtBA mole percent ranging from 0 to 18%. (**F**) Measured voltage of a commercial capacitor (1, 2.2, 3.3, 10, 22, 33, 100, 220, 330, and 1000 μF) charged with ac-to-dc signal converting circuit using PVDF-G18–based TENG.

of free space (8.854×10^{-12} F m^{-1}), and the gap distance (d_{gap}) of the TENG can be assigned as d_{gap} = 1 mm. The dielectric constant of the PVDF-G*n* film was obtained from the results, measured to be 9.1 to 16.5. It is clear that the potential increases with PtBA mole percent, meaning that the output power of the TENG is enhanced.

To show their practical application, we evaluated the capacitor charging characteristic of the TENGs, which were integrated with an ac-to-dc converting circuit, as shown in fig. S6A. The converting circuit consists of one rectifier, three low capacitors (3 × 0.001 μF), and one capacitor (1, 2.2, 3.3, 10, 22, 33, 100, 220, 330, and 1000 μF) to convert the output signal from ac to dc. When a vertical compressive force of 50 N under a frequency of 10 Hz was applied, the capacitors were charged up to approximately 4 V when a 1000-μF capacitor was used. It was also clearly seen that the capacitor charge by the PVDF-G18–based TENG was much faster and the charged voltage was twice larger, compared with those of pristine PVDF–based TENG (fig. S6B).

Figure 3 shows the flexibility and durability of the PVDF film–based TENG. To show this flexibility, we bent the films 3000 times, as shown in Fig. 3A, and measured the output current densities, as compared with those measured before the bending. As shown in Fig. 3B, neither TENG exhibited a significant change in the output current densities before or after bending, indicating that the films are quite stable in harsh environments. The PVDF-G18–based TENG still generated a higher output current than the pristine PVDF–based one. The output current density generated by the PVDF-G18–based TENG also did not appear to change significantly at 18,000 cycles during the test. This result reveals the robustness and mechanical durability of TENGs in practical settings.

The enhancement in output power due to grafting was analyzed in many ways because there are many factors influencing the output power, such as the surface roughness of the contact layers, the compressibility of the triboelectric materials, the dielectric properties, and the surface potentials (*16*, *17*, *23*, *31*). Furthermore, these factors may be interrelated to each other, meaning that the main reason for the enhancement was not easy to find. First, we evaluated the surface morphology of the PVDF-G*n* films measured using atomic force microscopy (AFM), as shown in fig. S7A. The root mean square roughness value was measured to be approximately 98.11 nm at the PVDF-G18,

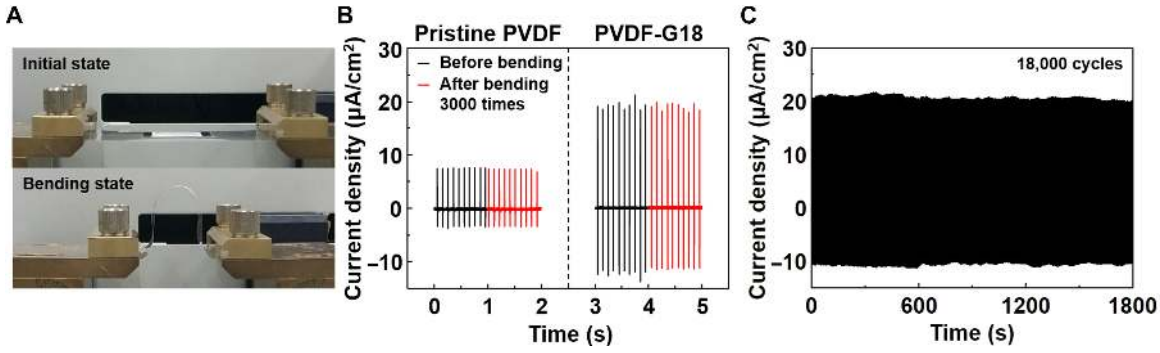

Fig. 3. Mechanical bending, stability, and durability test of PVDF-G*n*–based TENG. (**A**) Mechanical bending tests of the PVDF-based TENG. (**B**) Output current densities generated by pristine PVDF– and PVDF-G18–based TENGs before and after bending 3000 times. (**C**) Stability and durability test of the TENG under cycled compressive force of 50 N over 18,000 cycles.

and there was no significant change as the mole percent decreased from 18 to 0%, as shown in fig. S7A. We strove to minimize the effect of the roughness by casting the solution on a very flat SiO_2/Si substrate and peeling off the film to make a very flat PVDF surface because an important factor in enhancing the output performance of the TENG is to increase its surface roughness. These results may imply that the effect of the roughness on the output power is negligible.

The cross-sectional scanning electron microscopy (SEM) images of the PVDF-G*n* films with the grafting ratio are shown in fig. S7B. Here, the thickness of all films was fixed to approximately 30 μm. All films were quite porous, which is most likely due to the slow solvent removal process at low temperature (~60°C). These porous structures are effective in enhancing the output power because the output performance is significantly dependent on compressibility (*16*). Here, to measure the compressibility of the films, we evaluated resistance to deformation by external force using the Berkovich indenter, which induces a much higher local strain than uniaxial compression. The loading and unloading curves measured by the nanoindentation test on the PVDF-based films are shown in fig. S8. The nanoindentation results show that plastic collapse occurs in all samples during loading and unloading. The loading-unloading curves for PVDF-based films shown in fig. S8A indicate their repeatable plastic deformation, with the same displacement depth of approximately 1 μm when in uniaxial compression. On the basis of the nanoindentation test (fig. S8B), one can conclude that there is no change in the elastic modulus and hardness of PVDF-based films, meaning that the films exist with partially elastic recovery and not perfectly elastic recovery and are mixed via the elastic-plastic transition.

With two important factors excluded, we measured the frequency-dependent dielectric properties of the PVDF-based films over the frequency range of 10^2 to 10^6 Hz at room temperature, plotted in Fig. 4. To measure the dielectric constants, PVDF-based films were prepared on an Au/Si substrate, and Au as a top electrode was then deposited using an e-beam evaporator. For the pristine PVDF film, the dielectric constant was measured to be approximately 8.6 in the frequency range of 10^2 to 10^5 Hz, which is almost the same as in previous reports (*32*, *33*). There is a significant drop in the dielectric constant in the higher frequency range (10^5 to 10^6 Hz). This is because the dipole relaxation of the polymers cannot catch up with the external oscillating field. As the grafting ratios in the backbone increased, the dielectric constant gradually increased. In consequence, the PVDF-G18 shows a superior dielectric constant value of up to 16.5 (fig. S9). There is no significant change in the loss tangent (~0.03) of all samples, except those in the higher frequency range. This means that the dielectric constant values are quite reliable. In principle, the dielectric constant has a strong correlation with polarizability and free volume of the elements present in the materials, as formulated in the Clausius-Mossotti equation (*34*). The π-bonding and polar characteristics of the ester groups (–COO–) in the PtBA are able to not only hold relatively great polarizability but also increase the net dipole moment in the backbone. These are considered to be major factors contributing to the improvement of dielectric constant values in the graft copolymers (*34*).

To investigate the relationship between the dielectric constant and output performance of the TENG, we compared the output currents of PVDF-based TENGs as a function of measuring time, as plotted in Fig. 5A. The output current increases with the mole percent, as also shown in Fig. 3. Note that the time taken for the output to reach 90% of the final current also increases with the mole percent from 3.15 (±0.51) s to 14.48 (±0.58) s, as plotted in Fig. 5B. In general, in a film-type capacitor, the accumulated charges (Q) can be expressed as

$$Q = CV\left[1 - e^{-\frac{t}{RC}}\right] \quad (4)$$

where C, V, t, and R are the capacitance, input voltage, charging time, and resistance, respectively. Assuming that V is constant, C can be calculated using the equation $C = \varepsilon_0\varepsilon_r A/d$, where ε_0, ε_r, A, and d are the permittivity of free space (8.854×10^{-12} F m^{-1}), dielectric constant of the material, contact area (4 cm^2), and distance (30 μm) between the top and bottom electrodes, respectively. Thus, the charges can be expressed with the dielectric constant in Fig. 5C. As the dielectric constant doubles, the charges increase by two times and the saturation time also increases from 2.3 to 4.52 s, which agrees well with the experimental results. This indicates that the increase in the dielectric constant can enhance the maximum charge density that can be sustained on the surface of the dielectric.

Finally, we further measured the surface potential difference of the pristine PVDF and PVDF-G18 to understand an important parameter that can affect output performance (Fig. 6A) by the KPFM tools, compared to the Pt-coated Si tip. The surface potential values were calculated as −156 mV for the Au film and −370 mV for the PVDF film, whereas PVDF-G18 showed a relatively higher potential value of +260 mV. Assuming that the surface potential of Al is not changed during the full cycle, the measured surface potential values indicate that the difference in work function between Al and PVDF-G18 is

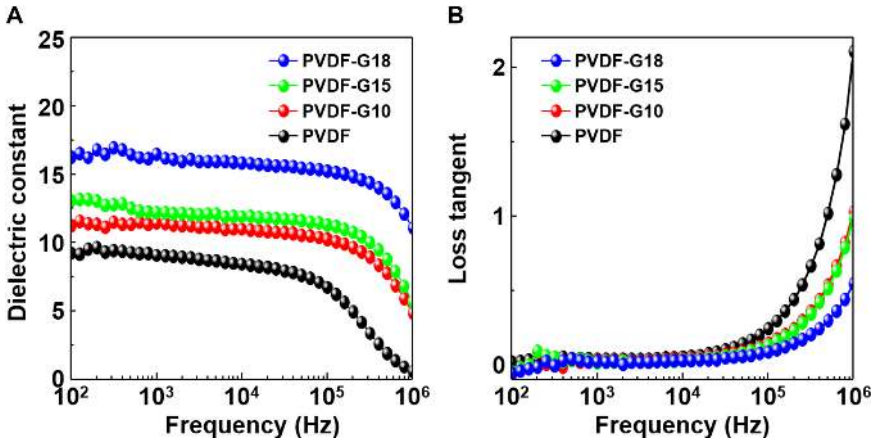

Fig. 4. Dielectric constant and loss tangent for PVDF-G*n* films. Frequency dependence of (**A**) dielectric constant values and (**B**) loss tangent for PVDF-based films with various PtBA mole percents ranging from 0 to 18%.

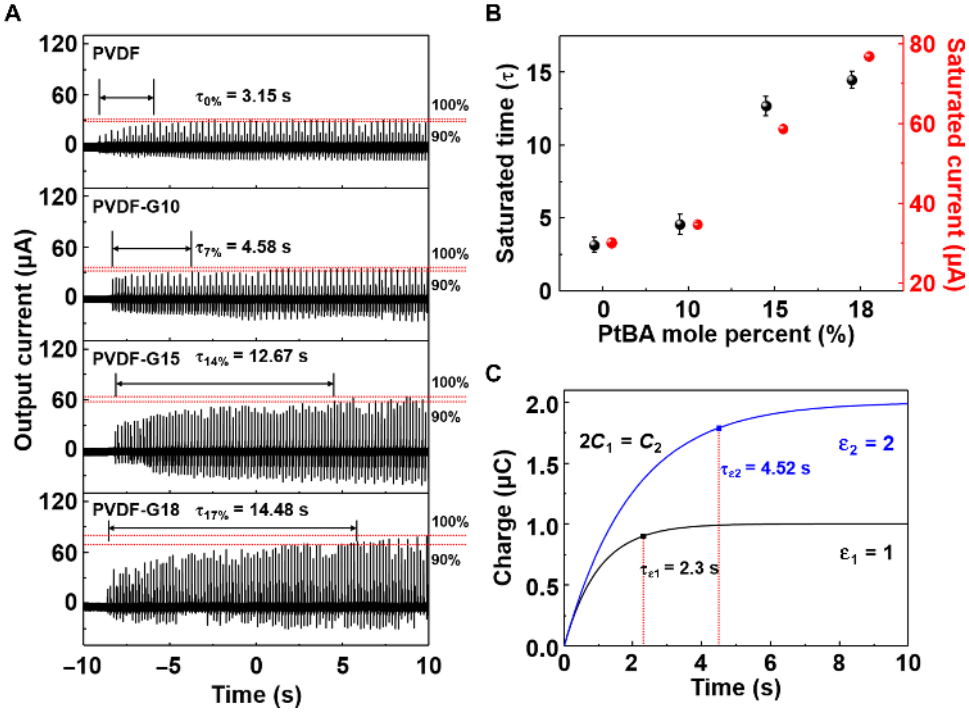

Fig. 5. Relationship between the dielectric constant and output performance of PVDF-G*n*–based TENG. (**A**) Measured output currents of the PVDF-based TENG with the grafting ratio. (**B**) Saturated time and output current as a function of the PtBA mole percent ranging from 0 to 18%. Error bars represent SEM. (**C**) Calculated charging time of the capacitor increases from 2.3 to 4.52 s with the increase of the dielectric constant.

smaller than that between Al and pristine PVDF, as shown in Fig. 6B. The decrease in work function with the grafting was supported by ultraviolet photoelectron spectroscopy (UPS) spectra, as shown in Fig. 6C. The work function can be determined from the difference between the incident light energy ($h\nu$ = 21.22 eV) and the energy of the secondary cutoff (E_{cutoff}) as $W = h\nu - (E_{cutoff} - E_F)$. The onset of the secondary electron peak shifted toward a lower binding energy by 1.19 eV for pristine PVDF and 0.48 eV for PVDF-G18, as compared with Al. On the basis of these results, the work function can be estimated to be approximately 5.55 (±0.19) eV and 4.84 (±0.16) eV in pristine PVDF and PVDF-G18, respectively (Fig. 6D), which agrees with the KPFM results. According to previous work, it is expected that the electron transfer from the Al to PVDF-G18 is not effective; therefore, the output performance of the TENG should be decreased because of the low electric potential generated between them.

The decrease of the work function in PVDF-G18 may be explained in terms of microstructural change. The crystalline properties of PVDF-based films were characterized by x-ray diffraction (XRD), compared with those of the PVDF film, and plotted in Fig. 7A. For the PVDF film, two representative peaks at 17.9° and 20.6° were observed. We thought that the two peaks would correspond to the (100) plane of the α phase and the (200) plane of the β phase, respectively. However, we found that the β (200) peak, which was

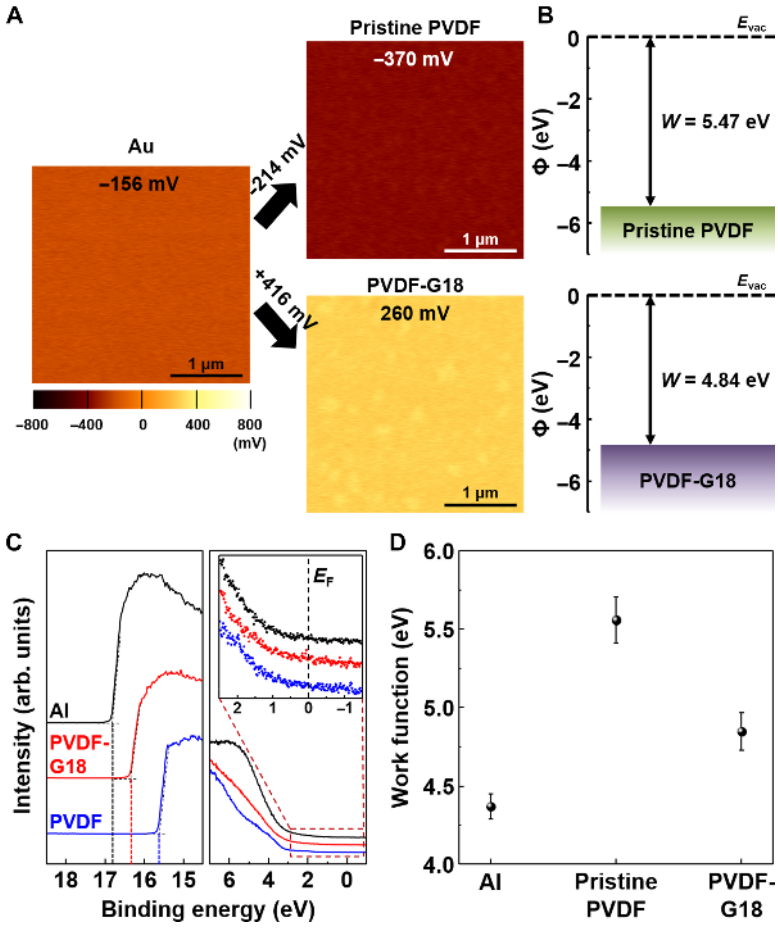

Fig. 6. Surface potential and UPS measurement of PVDF-G*n* films. (**A**) KPFM surface potential distribution images (3 μm × 3 μm) of Au, pristine PVDF, and PVDF-G18 films. (**B**) Work function values of pristine PVDF and PVDF-G18 films, obtained from the KPFM results. (**C**) UPS spectra and (**D**) the change in work function of Al, pristine PVDF, and PVDF-G18 films. Error bars represent SEM.

quite asymmetric, could be deconvoluted into two peaks, α (110) and β (200) (*35*), as shown in Fig. 7B. With the grafting, the peak intensity of α (110) significantly increased, whereas the β (200) peak almost disappeared. In general, the β phase is formed due to the rotation of the CF_2 chains when annealed (*36*). The chain mobility is strongly related to the structure of the molecules, molecular weight, chain length, etc. (*37*). This implies that the increase in the molecular weight and steric bulkiness can suppress the rotation of the chains in PVDF-G*n* films; therefore, β phase is not likely to be formed.

In general, the dipole moment originates from the asymmetric structure of the β phase in PVDF film and is directed toward the surface of the film. This is because CF_2 dipoles are rotated by the thermal energy and dipole moments that are uniformly aligned in parallel to the substrate (*38*, *39*). However, the β phases significantly decreased in PVDF-G*n* films. Thus, the increase in net dipole moments may be attributed to the formation of the polar molecules, that is, the polar β phase. In general, the change in the surface potential (ΔV) is defined through the Helmholtz equation (*40*)

$$\Delta V = 4\pi \frac{NP_0 \cos(\theta)}{A\varepsilon} \quad (5)$$

where A is the surface area, N is the number of molecules, P is the dipole moment, P_0 is the dipole moment of the free molecule in a vacuum, θ is the molecular tilt angle, and $\varepsilon = (P_0/P)$ is the effective dielectric constant of a molecular monolayer. The surface potential changes of $\Delta V = -214$ mV for pristine PVDF and $\Delta V = +416$ mV for PVDF-G18 result in the dipole moments of 1.26 and 3.41 D with opposite directions, respectively. By the KPFM result, the net dipole moment in PVDF-G*n* films is directed toward the substrate, opposite to that in the β phase, as shown in fig. S10. In general, the direction is influenced by the chain structure (*34*). In the β phase in PVDF film, the high dipole moment of $-CF_2$ units is aligned on the same side. As the grafting ratio increased, the extent of dipole orientation for the C–F bonds directed parallel to each other decreased, resulting in the opposite net dipole direction of the PVDF-G*n* film (*34*). Thus, one can conclude that the increase in the dielectric constant value is a dominant factor in the enhancement in the output power of the TENG.

On the basis of the measured surface potential of the PVDF film, for further enhancement in the output power, we poled the film at 100 MV m^{-1} for 30 min and aligned the dipole direction to increase the work function difference with the Al. Figure 8 shows the output voltages and the output currents, depending on the poling electric field direction. For pristine PVDF film, the TENG generated 65 V and 11 μA/cm^2 under forward bias and −14 V and −2.7 μA/cm^2 under

reverse bias. As the grafted PtBA reached 18%, the output voltage and current density were measured to be 105 V and 25 μA/cm^2 under forward bias and −39 V and −11 μA/cm^2 under reverse bias. The significant increase in the output power of PVDF-G*n* results from the positive charges on the surface of forward-polarized PVDF brought into contact with the aluminum, whereas the other side of its surface is covered by the back electrode.

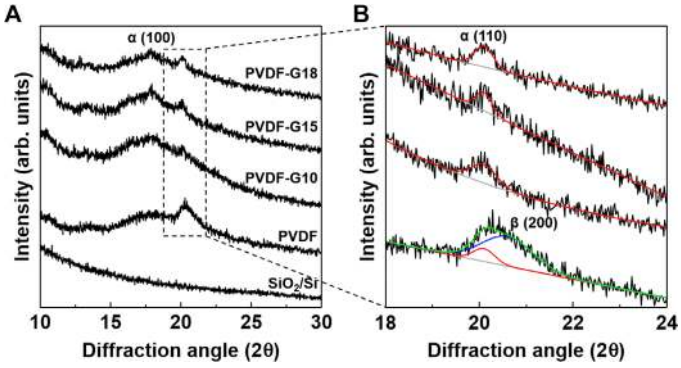

Fig. 7. XRD pattern of PVDF-G*n* films. (**A**) High-resolution XRD patterns of pristine PVDF and PVDF-G*n* films as a function of PtBA mole percent. (**B**) Expanded view of the second peak in (A). The peak can be deconvoluted into two peaks, α (110) (red) and β (200) (blue) phases.

CONCLUSION

In summary, we reported a facile approach to enhance the output power of TENG with the successful synthesis of PtBA-grafted PVDF copolymers for dielectric constant control. The copolymers were prepared using the ATRP technique, and the PtBA was grafted up to 18%. In high-resolution XRD spectra, it was found that the β phases significantly decreased; thus, the copolymers were mainly composed of α phases with an enhanced dipole moment by π-bonding and polar characteristics of the ester functional groups in the PtBA. As the grafting ratio increased to 18%, the dielectric constant values increased from 8.6 to 16.5 in the frequency range of 10^2 to 10^5 Hz, which we attributed to the increase of the net dipole moment, supported by the KPFM measurements. This increase in the dielectric constant increased the density of the charges that could be accumulated on the surface, generating output signals of 64.4 V and 18.9 μA/cm^2, twice the enhancement in both, compared to pristine PVDF–based nanogenerator. To prove this, we calculated the accumulated charges on the surface with different dielectric constant values, which showed an excellent correspondence with the measured output current values. The enhanced output performance is quite stable and reliable in harsh mechanical environments due to the high flexibility of the films. Further increase in the output signals to 105 V and 25 μA/cm^2, a 20-fold enhancement in output power, was also achieved by poling the film to align the dipole direction, which improved the charge-accepting characteristics by increasing the work function of the copolymer. The enhanced output power resulted in a much faster charging property.

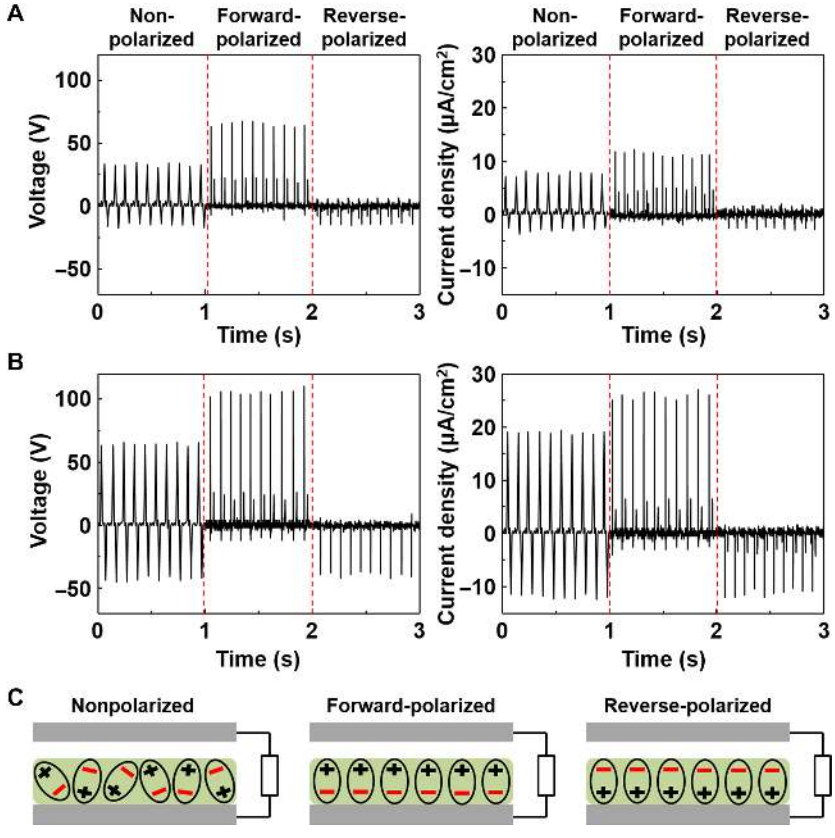

Fig. 8. Output performance depending on the poling electric field direction. Output voltages and current densities for (**A**) pristine PVDF–based and (**B**) PVDF-G18–based TENGs under different poling electric field directions. (**C**) Circuit diagrams and different performances among TENGs fabricated under different poling electric field directions.

MATERIALS AND METHODS

Materials and instruments

PVDF [KF1100; M_n = 168.8 kDa, polydispersity index (PDI) = 2.94] was purchased from Kureha. *tert*-Butyl acrylate (tBA) was purchased from Sigma-Aldrich and was passed through an aluminum oxide column to remove the inhibitor before use. Copper(I) chloride (CuCl, 99.999%) and 1,1,4,7,10,10-hexamethyltriethylenetetramine (HMTETA) were purchased from Alfa Aesar. 1-Methyl-2-pyrrolidone (NMP) was purchased from JUNSEI. All solvents were reagent grade, and all reagents were used as received. The molecular mass of PVDF and graft copolymers were measured by gel permeation chromatography (GPC) conducted at 23°C in *N*,*N*′-dimethylformamide (DMF) at a flow rate of 1 ml/min, using an Agilent 1260 Infinity GPC system equipped with a PLgel 5 μm Mixed B column (Polymer Laboratories) and differential refractive index detectors. Monodisperse PS standard (Polymer Laboratories) was used for calibration. ^{1}H NMR was performed in deuterated DMF, using a 400-MR DD2 (Agilent) 400-MHz spectrometer. The FTIR spectra were recorded on a 670-IR (Agilent) spectrophotometer.

Synthesis of PVDF-G*n* graft copolymers

PVDF (3.0 g) was dissolved in NMP (30 ml) at 60°C. Once the PVDF had completely dissolved in NMP, tBA (18.02 g, 93.5 mmol), CuCl (0.03 g, 0.202 mmol), and HMTETA (0.127 g, 0.367 mmol) were added to the PVDF solution at room temperature under an argon atmosphere. The reaction mixture was then heated at 120°C for a certain reaction time (either 12, 24, or 72 hours). After cooling to room temperature, the copolymer solution was poured into water/methanol (1:4, v/v) and filtered off. The precipitated copolymer was stirred overnight in a large volume of hexane. The copolymer was then recovered by filtration, redissolved in NMP, and precipitated into water/methanol (1:4, v/v). Last, the graft copolymers were dried under a vacuum. For ^{1}H NMR (400 MHz, C_3D_7NO), δ (ppm) values were as follows: 2.9 to 3.2 (br, 2H, $-CF_2-CH_2-CF_2-CH_2-$), 2.3 to 2.5 (br, 2H, $-CF_2-CH_2-CH_2-CF_2-$), and 1.4 to 1.65 [br, 9H, $-C(CH_3)_3$]. For PVDF-G10, the parameters used were as follows: M_n = 180.0 kDa, PDI = 1.58; for PVDF-G15, M_n = 201.8 kDa, PDI = 1.56; and for PVDF-G18, M_n = 218.5 kDa, PDI = 1.47.

Production of PVDF-based TENG

In the experiment, the synthesized PVDF-G*n* solution was first cast into a film shape in a blocking layer on an SiO_2/Si substrate and dried in the atmosphere at 60°C for 10 min to remove the DMF solution. This layer was then maintained at 90°C for 5 hours and cooled at room temperature. After the PVDF-G*n* film layer was peeled off from the substrate, the PVDF-G*n* film of 30 μm was obtained. To fabricate the TENG, a Kapton film was glued between Al foil and PVDF-G*n* film, followed by the attachment of Al electrode on the opposite side of the Kapton film, which acts as the top layer. The spacer between the bottom electrode and the PVDF-G*n* film was made of four springs with a length of 5 mm in each corner. Last, PVDF-G*n*–based TENGs were obtained. The effective area and gap distance of both PVDF and PVDF-G*n* films were 2 cm × 2 cm and 1 mm, respectively.

Characterization and measurements

The morphologies of PVDF-based films were further characterized by a field emission SEM. The dielectric constants of the PVDF-based films were measured by an impedance analyzer (Agilent) over the frequency range of 10^2 to 10^6 Hz at room temperature. A pushing tester (model no. ET-126-4, Labworks Inc.) was used to create vertical compressive strain in the TENG. A Tektronix DPO 3052 digital phosphor oscilloscope and a low-noise current preamplifier (model no. SR570, Stanford Research Systems Inc.) were used for electrical measurements. Nanoindentation tests were carried out at a constant indentation strain rate of 0.05 s^{-1}, with a maximum indentation depth of 20 μm, with a Berkovich indenter, using the DCM II module in Nanoindenter G200 (Agilent). The KPFM measurements were carried out using Park Systems XE-100 with Pt/Cr-coated silicon tips (tip radius, 25 nm; force constant, 3 N m^{-1}; and resonance frequency, 75 kHz). KPFM images (3 μm × 3 μm) were scanned at a scanning speed of 0.5 Hz in the noncontact mode with a 2-V_{ac} signal with a frequency of 17 kHz. UPS (ESCALAB 250Xi, Thermo Fisher) was performed using the He I ($h\nu$ = 21.2 eV) photon line of a He discharge lamp under ultrahigh vacuum conditions for measurement of the work function.

SUPPLEMENTARY MATERIALS

Supplementary material for this article is available at http://advances.sciencemag.org/cgi/content/full/3/5/e1602902/DC1

fig. S1. Output voltages of PVDF-based TENGs.
fig. S2. Output performances of different polymer-based TENGs.
fig. S3. Output performance of pristine PVDF–based TENG with the resistance of external loads.
fig. S4. Average current density and charge density.
fig. S5. Calculated electrostatic potentials.
fig. S6. Capacitor charging properties of pristine PVDF–based TENGs.
fig. S7. AFM and SEM images of the PVDF-G*n* films.
fig. S8. Nanoindentation test for the PVDF-G*n* films.
fig. S9. Dielectric constant of PVDF-G*n* films according to PtBA mole percents.
fig. S10. Structures of PVDF and PVDF-G*n*.

REFERENCES AND NOTES

1. W. J. Sarjeant, J. Zirnheld, F. W. MacDougall, Capacitors. *IEEE Trans. Plasma Sci.* **26**, 1368–1392 (1998).
2. Y. Cao, P. C. Irwin, K. Younsi, The future of nanodielectrics in the electrical power industry. *IEEE Trans. Dielectr. Electr. Insul.* **11**, 797–807 (2004).
3. S. Ducharme, An inside-out approach to storing electrostatic energy. *ACS Nano* **3**, 2447–2450 (2009).
4. B. Chu, X. Zhou, K. Ren, B. Neese, M. Lin, Q. Wang, F. Bauer, Q. M. Zhang, A dielectric polymer with high electric energy density and fast discharge speed. *Science* **313**, 334–336 (2006).
5. S. Wu, W. Li, M. Lin, Q. Burlingame, Q. Chen, A. Payzant, K. Xiao, Q. M. Zhang, Aromatic polythiourea dielectrics with ultrahigh breakdown field strength, low dielectric loss, and high electric energy density. *Adv. Mater.* **25**, 1734–1738 (2013).
6. Q. Chen, Y. Shen, S. Zhang, Q. M. Zhang, Polymer-based dielectrics with high energy storage density. *Annu. Rev. Mater. Res.* **45**, 433–458 (2015).
7. M.-H. Yoon, H. Yan, A. Facchetti, T. J. Marks, Low-voltage organic field-effect transistors and inverters enabled by ultrathin cross-linked polymers as gate dielectrics. *J. Am. Chem. Soc.* **127**, 10388–10395 (2005).
8. M. E. Roberts, N. Queraltó, S. C. B. Mannsfeld, B. N. Reinecke, W. Knoll, Z. Bao, Cross-linked polymer gate dielectric films for low-voltage organic transistors. *Chem. Mater.* **21**, 2292–2299 (2009).
9. M. T. Dang, L. Hirsch, G. Wantz, P3HT:PCBM, best seller in polymer photovoltaic research. *Adv. Mater.* **23**, 3597–3602 (2011).
10. L. Huo, S. Zhang, X. Guo, F. Xu, Y. Li, J. Hou, Replacing alkoxy groups with alkylthienyl groups: A feasible approach to improve the properties of photovoltaic polymers. *Angew. Chem.* **123**, 9871–9876 (2011).
11. S. Dadbin, M. Frounchi, M. H. Saeid, F. Gangi, Molecular structure and physical properties of E-beam crosslinked low-density polyethylene for wire and cable insulation applications. *J. Appl. Polym. Sci.* **86**, 1959–1969 (2002).
12. Z. Li, J. Chen, J. Yang, Y. Su, X. Fan, Y. Wu, C. Yu, Z. L. Wang, β-Cyclodextrin enhanced triboelectrification for self-powered phenol detection and electrochemical degradation. *Energy Environ. Sci.* **8**, 887–896 (2015).
13. J.-H. Kim, J. Chun, J. W. Kim, W. J. Choi, J. M. Baik, Self-powered, room-temperature electronic nose based on triboelectrification and heterogeneous catalytic reaction. *Adv. Funct. Mater.* **25**, 7049–7055 (2015).

14. S. Wang, L. Lin, Z. L. Wang, Nanoscale triboelectric-effect-enabled energy conversion for sustainably powering portable electronics. *Nano Lett.* **12**, 6339–6346 (2012).
15. Y. Yang, H. Zhang, Y. Liu, Z.-H. Lin, S. Lee, Z. Lin, C. P. Wong, Z. L. Wang, Silicon-based hybrid energy cell for self-powered electrodegradation and personal electronics. *ACS Nano* **7**, 2808–2813 (2013).
16. J. Chun, J. W. Kim, W.-s. Jung, C.-Y. Kang, S.-W. Kim, Z. L. Wang, J. M. Baik, Mesoporous pores impregnated with Au nanoparticles as effective dielectrics for enhancing triboelectric nanogenerator performance in harsh environments. *Energy Environ. Sci.* **8**, 3006–3012 (2015).
17. J. Chen, H. Guo, X. He, G. Liu, Y. Xi, H. Shi, C. Hu, Enhancing performance of triboelectric nanogenerator by filling high dielectric nanoparticles into sponge PDMS film. *ACS Appl. Mater. Interfaces* **8**, 736–744 (2016).
18. G. Zhu, Z.-H. Lin, Q. Jing, P. Bai, C. Pan, Y. Yang, Y. Zhou, Z. L. Wang, Toward large-scale energy harvesting by a nanoparticle-enhanced triboelectric nanogenerator. *Nano Lett.* **13**, 847–853 (2013).
19. G. Zhu, C. Pan, W. Gu, C.-Y. Chen, Y. Zhou, R. Yu, Z. L. Wang, Triboelectric-generator-driven pulse electrodeposition for micropatterning. *Nano Lett.* **12**, 4960–4965 (2012).
20. Z. Zhao, X. Pu, C. Du, L. Li, C. Jiang, W. Hu, Z. L. Wang, Freestanding flag-type triboelectric nanogenerator for harvesting high-altitude wind energy from arbitrary directions. *ACS Nano* **10**, 1780–1787 (2016).
21. P. Bai, G. Zhu, Y. S. Zhou, S. Wang, J. Ma, G. Zhang, Z. L. Wang, Dipole-moment-induced effect on contact electrification for triboelectric nanogenerators. *Nano Res.* **7**, 990–997 (2014).
22. P. Bai, G. Zhu, Z.-H. Lin, Q. Jing, J. Chen, G. Zhang, J. Ma, Z. L. Wang, Integrated multilayered triboelectric nanogenerator for harvesting biomechanical energy from human motions. *ACS Nano* **7**, 3713–3719 (2013).
23. Y. S. Zhou, S. Wang, Y. Yang, G. Zhu, S. Niu, Z.-H. Lin, Y. Liu, Z. L. Wang, Manipulating nanoscale contact electrification by an applied electric field. *Nano Lett.* **14**, 1567–1572 (2014).
24. K. Y. Lee, J. Chun, J.-H. Lee, K. N. Kim, N.-R. Kang, J.-Y. Kim, M. H. Kim, K.-S. Shin, M. K. Gupta, J. M. Baik, S.-W. Kim, Hydrophobic sponge structure-based triboelectric nanogenerator. *Adv. Mater.* **26**, 5037–5042 (2014).
25. A. V. Shirinov, W. K. Schomburg, Pressure sensor from a PVDF film. *Sens. Actuators A Phys.* **142**, 48–55 (2008).
26. Y. Song, Y. Shen, H. Liu, Y. Lin, M. Li, C.-W. Nan, Enhanced dielectric and ferroelectric properties induced by dopamine-modified $BaTiO_3$ nanofibers in flexible poly(vinylidene fluoride-trifluoroethylene) nanocomposites. *J. Mater. Chem.* **22**, 8063–8068 (2012).
27. M. Li, H. J. Wondergem, M.-J. Spijkman, K. Asadi, I. Katsouras, P. W. M. Blom, D. M. de Leeuw, Revisiting the δ-phase of poly(vinylidene fluoride) for solution-processed ferroelectric thin Films. *Nat. Mater.* **12**, 433–438 (2013).
28. E. Fernández, C. Mijangos, J.-M. Guenet, M. T. Cuberes, D. López, New hydrogels based on the interpenetration of physical gels of agarose and chemical gels of polyacrylamide. *Eur. Polym. J.* **45**, 932–939 (2009).
29. F. Guan, L. Yang, J. Wang, B. Guan, K. Han, Q. Wang, L. Zhu, Confined ferroelectric properties in poly(vinylidene fluoride-*co*-chlorotrifluoroethylene)-*graft*-polystyrene graft copolymers for electric energy storage applications. *Adv. Funct. Mater.* **21**, 3176–3188 (2011).
30. Z.-H. Lin, G. Cheng, Y. Yang, Y. S. Zhou, S. Lee, Z. L. Wang, Triboelectric nanogenerator as an active UV photodetector. *Adv. Funct. Mater.* **24**, 2810–2816 (2014).
31. F.-R. Fan, L. Lin, G. Zhu, W. Wu, R. Zhang, Z. L. Wang, Transparent triboelectric nanogenerators and self-powered pressure sensors based on micropatterned plastic films. *Nano Lett.* **12**, 3109–3114 (2012).
32. Z.-M. Dang, Y.-H. Lin, C.-W. Nan, Novel ferroelectric polymer composites with high dielectric constants. *Adv. Mater.* **15**, 1625–1629 (2003).
33. B. Luo, X. Wang, Y. Wang, L. Li, Fabrication, characterization, properties and theoretical analysis of ceramic/PVDF composite flexible films with high dielectric constant and low dielectric loss. *J. Mater. Chem. A* **2**, 510–519 (2014).
34. Z. Ahmad, Polymer dielectric materials, in *Dielectric Material*, M. A. Silaghi, Ed. (Intech, 2012), pp. 3–26.
35. H. Yu, T. Huang, M. Lu, M. Mao, Q. Zhang, H. Wang, Enhanced power output of an electrospun PVDF/MWCNTs-based nanogenerator by tuning its conductivity. *Nanotechnology* **24**, 405401 (2013).
36. R. Gregorio Jr., M. Cestari, Effect of crystallization temperature on the crystalline phase content and morphology of poly(vinylidene fluoride). *J. Polym. Sci. B Polym. Phys.* **32**, 859–870 (1994).
37. L. Xu, V. Selin, A. Zhuk, J. F. Ankner, S. A. Sukhishvili, Molecular weight dependence of polymer chain mobility within multilayer films. *ACS Macro Lett.* **2**, 865–868 (2013).
38. Z. Hu, M. Tian, B. Nysten, A. M. Jonas, Regular arrays of highly ordered ferroelectric polymer nanostructures for non-volatile low-voltage memories. *Nat. Mater.* **8**, 62–67 (2009).
39. S. Satapathy, S. Pawar, P. K. Gupta, K. B. R. Varma, Effect of annealing on phase transition in poly(vinylidene fluoride) films prepared using polar solvent. *Bull. Mater. Sci.* **34**, 727–733 (2011).
40. A. Henning, G. Günzburger, R. Jöhr, Y. Rosenwaks, B. Bozic-Weber, C. Housecroft, E. C. Constable, E. Meyer, T. Glatzel, Kelvin probe force microscopy of nanocrystalline TiO_2 photoelectrodes. *Beilstein J. Nanotechnol.* **4**, 418–428 (2013).

Acknowledgments

Funding: This work was supported by the Samsung Research Funding Center of Samsung Electronics under project number SRFC-TA1403-06. **Author contributions:** J.W.L., H.J.C., and J.C. conceived the idea, analyzed the data, and wrote the manuscript. K.N.K. and S.K. conducted output measurements and prepared the figures. C.W.A., I.W.K., J.-Y.K., and S.-W.K. provided advice for the research and revised the manuscript. C.Y. and J.M.B. conceived and supervised this study and provided intellectual and technical guidance. All authors discussed the results and wrote and commented on the manuscript. **Competing interests:** The authors declare that they have no competing interests. **Data and materials availability:** All data needed to evaluate the conclusions in the paper are present in the paper and/or the Supplementary Materials. Additional data related to this paper may be requested from the authors.

Submitted 20 November 2016
Accepted 28 March 2017
Published 26 May 2017
10.1126/sciadv.1602902

Citation: J. W. Lee, H. J. Cho, J. Chun, K. N. Kim, S. Kim, C. W. Ahn, I. W. Kim, J.-Y. Kim, S.-W. Kim, C. Yang, J. M. Baik, Robust nanogenerators based on graft copolymers via control of dielectrics for remarkable output power enhancement. *Sci. Adv.* **3**, e1602902 (2017).

Robust nanogenerators based on graft copolymers via control of dielectrics for remarkable output power enhancement

Jae Won Lee, Hye Jin Cho, Jinsung Chun, Kyeong Nam Kim, Seongsu Kim, Chang Won Ahn, Ill Won Kim, Ju-Young Kim, Sang-Woo Kim, Changduk Yang and Jeong Min Baik (May 26, 2017)

Sci Adv 2017, 3:.
doi: 10.1126/sciadv.1602902